Published in: *Micromachined Devices and Components IV, Proc SPIE.,* **Vol 3514** , pp. 171-178

Characterization Techniques for Surface-Micromachined Devices

William P. Eaton, Norman F. Smith, Lloyd Irwin, Danelle M. Tanner
Sandia National Laboratories, Mail Stop 1081, Albuquerque, NM 87185

ABSTRACT

Using a microengine as the primary test vehicle, we have examined several aspects of characterization. Parametric measurements provide fabrication process information. Drive signal optimization is necessary for increased microengine performance. Finally, electrical characterization of resonant frequency and quality factor can be more accurate than visual techniques.

1. INTRODUCTION

Recent developments in surface-micromachining indicate a promising future for both microsensors and microactuators. A topic of interest for many researchers is characterizing these new devices. Characterization provides valuable information throughout the life cycle of a part which can be used for design verification, fabrication process monitoring, parameter extraction, and finally device lifetime.

The focus of this paper will be on microactuators, which were built in Sandia's SUMMiT 4-level polysilicon process [1,2,3]; additional data will be presented on devices built in Sandia's MEMS-CMOS integrated technology [3,4].

A number of elements are required in order to successfully create and operate a surface micromachined device. In this paper we will examine some of the experimental infrastructure required to test completed devices, a drive signal case study, standard parametrics measurements, and electrical measurements of resonant frequency and quality factor.

2. EXPERIMENTAL SETUP

The Sandia microengine is a basic building block for a number of complex actuators. Shown in Figure 1, it consists of two orthogonal comb drives attached to a pinion gear by linkage arms. Since the comb drives exhibit inherently linear motion, and a net circular motion is desired, the magnitude and phase of the drive signals must be optimized. These ideal drive signals have been reported elsewhere [5,6,7]. They account for the electrostatic forces of the comb drives, the restoring force of the folded comb drive springs, and the damping force associated with air damping. Furthermore, tangential and radial forces at the gear are included. The net equations generated by this ideal model are not simple sine waves, as shown in Figure 2.

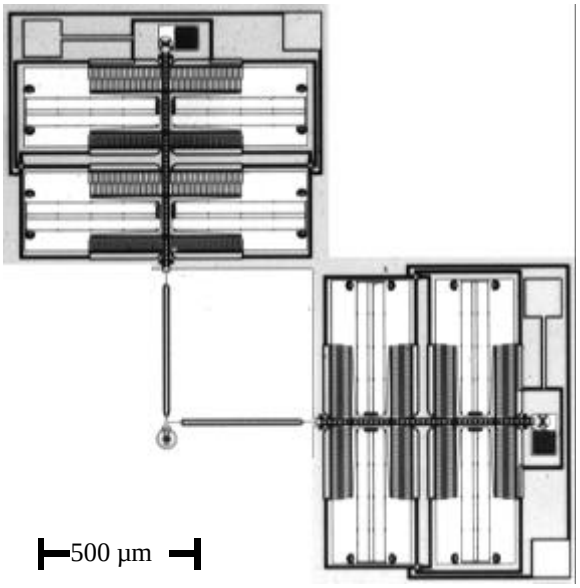

Figure 1. Photomicrograph of Sandia microengine.

Arbitrary waveform generators are needed to apply the proper electrostatic drive signals to the microengine. There are a total of four signals to be applied: up, down, right, and left (or $+y$, $-y$, $+x$, and $-x$, respectively). This

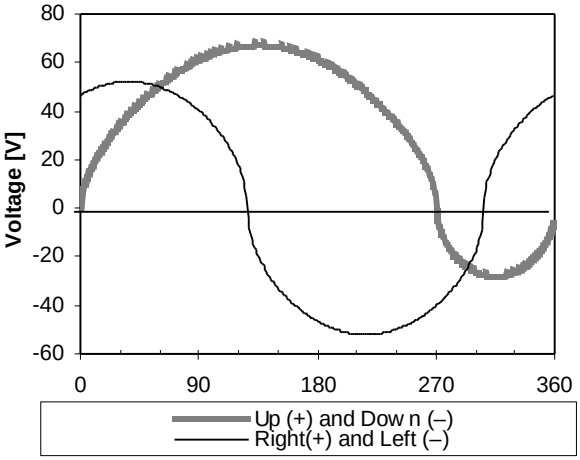

Figure 2. Ideal microengine drive signals. Positive lobes correspond to up and right signals. Negative lobes correspond to down and left signals. Note the angular and amplitude asymmetry in the up/down drive signals.

requires four arbitrary waveform generators. Custom software has been developed, *Super μDriver*, which automatically calculates drive signals based on the idealized model and downloads them to either a Pragmatic 2414A arbitrary waveform generator or a National Instruments AT-AO-10 ten channel analog output card.

Since up and down, left and right pairs do not overlap in the time domain, they can be generated with two generators, with up and down, left and right pairs corresponding to positive and negative lobes of the signals (Figure 3). By passing these composite signals through an inexpensive active rectifier circuit [8], the positive and negative lobes are split into their channels, and only two arbitrary waveform generators are required.

Relatively high voltages (60-80 V) are required to operate comb drives. Since typical waveform generators are unable to generate these signal levels, amplification is required. We have implemented this using Apex PA88A high voltage low power operation amplifiers in a circuit which supplies a fixed gain of 15.

Packaged parts are operated and inspected using either the Sandia High-volume Measurement of Micromachine Reliability (SHiMMeR) test system [9,10], which allow simulataneous operation and serial inspection of multiple packaged parts. This is useful for large-scale screening or characterization of parts. Typically, microengine dice are packaged in 24 pin ceramic DIPs. Microscope cover slides are taped over the package well to allow optical inspection. Optical inspections are either performed by a human operator or in some cases analytical data is extracted from a video camera and image analysis software.

3. PARAMETRIC MEASUREMENTS

Monitoring parametric parameters of test structures provides valuable information on the fabrication process. Routine measurements that are done at Sandia include:

- sheet resistance of polysilicon layers
- thin film stress
- free beam length
- resonant frequency of simple comb drives
- microengine functionality

Variation in sheet resistance of van der Pauw test structures in polysilicon may indicate problems with control of the dopant level, polysilicon microstructure variation, or over- or under- sizing of geometric features during patterning steps.

Thin film stress is a concern for most surface-micromachined devices. Compressive stress can cause buckling, while tensile stress can result in lowered device sensitivity. For these reasons, it is usually desirable to have built-in thin film stresses be as small and possible and be tensile. We use 'bow tie' structures similar to those reported by Gianchandani and Najafi [11]. The advantage of these structures is that they continuously measure both tensile and compressive strain with a single structure.

The last three tests, microengine functionality, comb drive resonant frequency, and free beam length, all yield information on possible stiction. If the microengine and the comb drive actuate under electrostatic stimulus, then they are free of stiction. Subtle processing variations may also be manifest in device behavior.

Comb drive resonant frequency is commonly measured by using a 'blur envelope' technique: as the frequency of the electrical drive signals to the comb drives is swept, the amount of comb drive deflection changes. The deflection goes through a maximum at the resonant frequency. The deflection is viewed on a video monitor. At high speeds ($\gtrsim$ 1kHz), the motion is blurred. The amplitude of deflection is determine by the amount of blur or the size of the blur envelope. This technique is relatively insensitive and is being replaced by an electrical technique described later in this paper.

The free beam length of cantilever beams is indicative of the quality of the release etching process. When viewed under an interferometer, it can be quickly determined whether a cantilever beam is free or stuck to the substrate. Shorter beams will tend to be free, while longer beams are more likely to be stuck. The length at which this transition occurs is called the free beam length, and is longer for a good release process.

4. DRIVE SIGNAL CASE STUDY: FLEX JOINTS VS. PIN JOINTS

As discussed in the EXPERIMENTAL SETUP section, application of proper drive signals is crucial to smooth operation of microengines. The model accounts for the restoring springs in the comb drives, the comb drive electrostatic force constant, and air damping. A second order effect in the operation of the microengine is the type of joint used to link the arms on a microengine to the comb drives. Two types of joints have been commonly used, pin joints and flex joints. Pin joints are similar to common macro-mechanical pin joints and are assumed to present no resistance to bending. In practice, however, pin joints will experience friction and may pose a reliability risk to the microengine. The microengine shown in Figure 1 and Figure 3 has flex joints, which are regions where the arm width is locally decreased, which caused a reduced resistance to bending. While these joints will not experience mechanical friction, they will tend to behave as torsional springs. Several experiments were done to determine whether these torsional springs had a significant impact on microengine behavior, or whether they could be 'lumped' together with the springs of the comb drives.

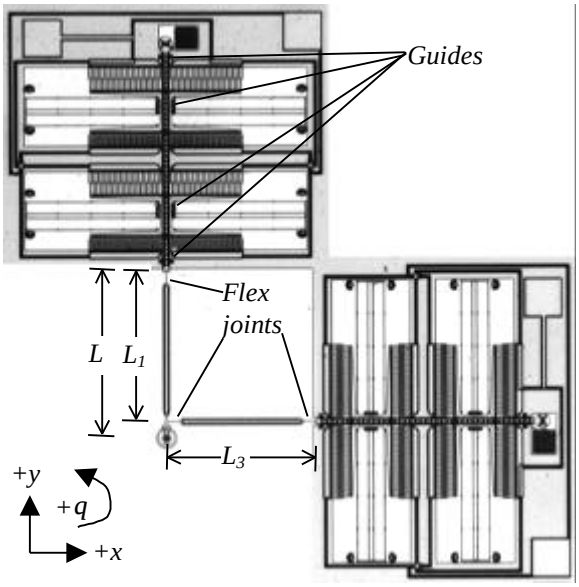

Figure 3. Photomicrograph of microengine labeled with dimensions, sign conventions, and salient features. Guides are shown for the y comb only and only on the right side of the shuttle.

Image analysis is an effective technique for evaluating the efficacy of drive signals. Two simple measurements are measurement of *x*-*y* position on a 'gearless' engine or angle vs. time on a geared engine. In the first measurement, a microengine without the drive gear is used. If proper drive signals are used, the linkage arms should sweep out a perfect circle, with a radius of the drive gear.

In the second measurement, the angle vs. time of the drive gear is monitored. This can be done by using a strobing technique. For a microengine at constant angular velocity, the angle vs. time should be a straight line.

Full derivations of the drive signals have been reported elsewhere [5,6,7], and the results are summarized here for convenience. For a microengine with no flex joints, the drive signal equations are

$$V_x^{\,2} = \frac{1}{g}\frac{kr}{a}\left\{\begin{array}{l}\dfrac{g^2}{w_0^{\,2}}\left[\left(\ddot{q}+2\dot{d}\dot{q}\right)\cos(q)-\dot{q}^{\,2}\sin q\right]\\ +\left(\dfrac{F_r}{kr}+g^2\right)\sin q+\dfrac{F_l}{kr}\cos q\end{array}\right\} \quad (1)$$

and

$$V_y^{\,2} = \frac{kr}{a}\left\{\begin{array}{l}\dfrac{1}{w_0^{\,2}}\left[\left(\ddot{q}+2\dot{d}\dot{q}\right)\sin(q)-\dot{q}^{\,2}\cos q\right]\\ +\left(\dfrac{F_r}{kr}+1\right)\cos q+\dfrac{F_l}{kr}\sin q\end{array}\right\}, \quad (2)$$

where V_x and V_y are *x* voltage (right and left) and *y* voltage (up and down), respectively. The variables *k*, *a*, and w_0 are the spring constant, electrostatic force constant, and resonant frequency, respectively, associated with the comb drives. The radius of the gear is represented by *r* and the radial and tangential forces on the gear are F_l and F_r, respectively. The term g is the ratio of L_1 to L_3 (see Figure 3). The gear angle, angular velocity and angular acceleration are given by q, $\dot{q}$, and $\ddot{q}$ respectively.

If the flex joints are taken into account, the drive signal equations become

$$V_x^{\,2} = \frac{1}{g}\frac{kr}{a}\left\{\begin{array}{l}\dfrac{g^2}{w_0^{\,2}}\left[\left(\ddot{q}+2\dot{d}\dot{q}\right)\cos(q)-\dot{q}^{\,2}\sin q\right]\\ +\left(\dfrac{1}{1-b_x b_y}\dfrac{F_r}{kr}+g^2\right)\sin q+\dfrac{F_l}{kr}\cos q\\ +\dfrac{g l_{2\,\mathrm{mod}}}{kr}\end{array}\right\} \quad (3)$$

and

$$V_y^{\,2} = \frac{kr}{a}\left\{\begin{array}{l}\dfrac{1}{w_0^{\,2}}\left[\left(\ddot{q}+2\dot{d}\dot{q}\right)\sin(q)-\dot{q}^{\,2}\cos q\right]\\ +\left(\dfrac{F_r}{kr}+1\right)\cos q+\dfrac{F_l}{kr}\sin q+\dfrac{l_{1\,\mathrm{mod}}}{kr}\end{array}\right\}, \quad (4)$$

where b_x and b_y are given by

$$b_x \approx \frac{r}{L}\sin q, \qquad b_y \approx \frac{r}{L_3}(1-\cos q) \quad (5)$$

where *L* and L_3 are the lengths of the *y* and *x* arms respectively. The terms containing l are given by

$$\frac{g l_{2\,\mathrm{mod}}}{kr} = \frac{g}{(1-b_x b_y)L_1 L_3}\left[\begin{array}{l}LL_3 b_x\left(F_l\sin q - F_r\cos q\right)\\ +LL_3\left(F_r\sin q + F_l\cos q\right)\\ +L_1 b_x\dfrac{k_{flex}}{kr}\left(b_x+2b_y\right)\\ +L_3\dfrac{k_{flex}}{kr}\left(b_y+2b_x\right)\end{array}\right] \quad (6)$$

and

$$\frac{l_{1\,\mathrm{mod}}}{kr} = \frac{1}{(1-b_x b_y)L_1 L_3}\left[\begin{array}{l}LL_3 b_y\left[\begin{array}{l}\left(F_l - F_r b_x\right)\cos q\\ +\left(F_r + F_l b_x\right)\sin q\end{array}\right]\\ +L_3 b_y\dfrac{k_{flex}}{kr}\left(b_y+2b_x\right)\\ +L_1\dfrac{k_{flex}}{kr}\left(b_x+2b_y\right)\end{array}\right]. \quad (7)$$

To determine the lumped kr/a and k_{flex}/kr terms, a gearless engine can be biased with DC voltages. Without a gear, the engine is no longer constrained to move in a circle. If, however, an operator applies the appropriate static voltages, the engine can be made to sweep out a circle of appropriate radius. In this case, all dy-

namic terms are nulled, and so are F_l and F_r. This simplifies the drive signal equations greatly and they become

$$V_x^2 = \frac{kr}{a} g\sin q \tag{8}$$

$$V_y^2 = \frac{kr}{a}(1-\cos q) \tag{9}$$

for the 'no flex joint' equations and

$$V_x^2 = \frac{kr}{a}\left\{ g\sin q + \frac{l_{2\mathrm{mod}}}{kr} \right\} \tag{10}$$

$$V_y^2 = \frac{kr}{a}\left\{ 1-\cos q + \frac{l_{1\mathrm{mod}}}{kr} \right\} \tag{11}$$

for the flex joint equations. By using equations 8-11 along with experimental data, the kr/a and k_{flex}/kr terms can be extracted. The results of one such measurement are shown in Figure 4 on a flex jointed engine. In the case of the 'no flex fit' the effect of the flex joints is assumed to be negligible and the experimental data are fit to Equations 1 and 2. The 'flex fit' trace was determined using Equations 3 and 4. The right/left data show that the flex joint equations fit the data better than the non flex joint equations.

While the static flex joint equations fit the static data better, it still must be determined how the dynamic equations fit the dynamic data. To do this, gearless engines were again used, but this time with the dynamic equations. Engines were operated at 100 Hz, and an Olympus ALS12000S strobe was used in conjunction with a frame capture card to acquire a series of images. The images were then processed using software (Impuls Vision) to determine the position of the arm on the gearless engine. For this setup, proper drive signals should have yielded perfect circular motion.

Figure 5 shows the results of a gearless engine with a known problem of linear clamping. Linear clamping occurs when interdigitated combs are engaging and suddenly snap into full engagement. Both the flex and no flex equations yielded poor results.

Linear clamping can be avoided if the range of motion of the comb drives is restricted. This can effectively done by lowering r by 75% from 17 µm to 12.75 µm. The results are shown in Figure 6. Much better circularity is observed, but no significant difference between flex joint and no flex joint equations are seen. This could lead to the possible conclusion that there is no significant difference in practice between the two equation sets. However, for smaller radii circles, the flex joints do not flex as much and hence their contribution to the forces on the microengine is smaller.

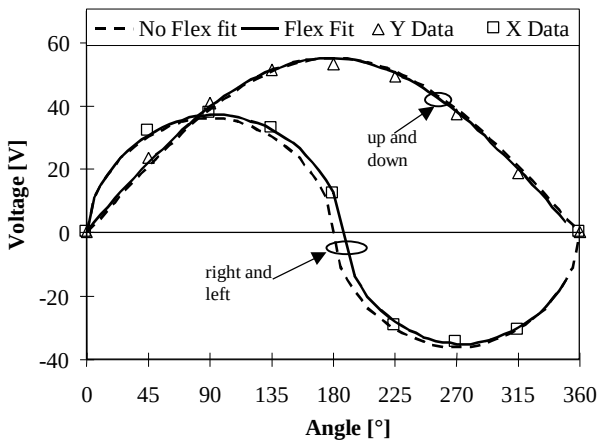

Figure 4. Static data and curve fits for a gearless microengine. The flex fit curves show better agreement with right/left data than the no flex fit curves. For flex fit: kr/a = 1475, k_{flex}/kr = 365. **For no flex fit:** kr/a = 1513**.**

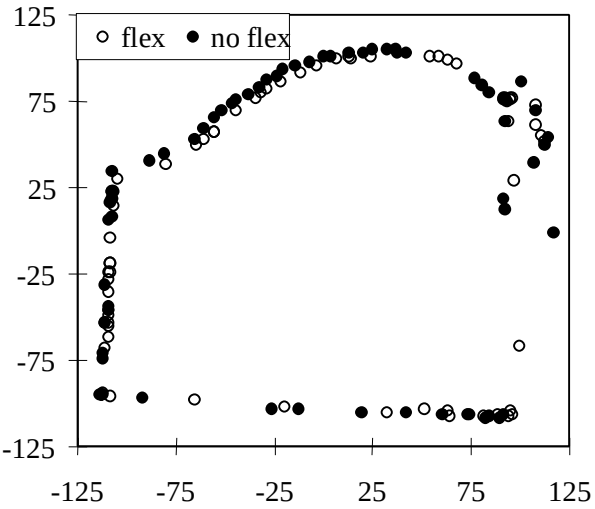

Figure 5. Position map of gearless engine with linear clamping and radius set to 17 µm. Horizontal and vertical axes are in pixels. 1 pixel » 3 µm.

To resolve this problem, a newer microengine design was characterized which did not exhibit linear clamping. Unfortunately the new design exhibited a new problem which was excess friction in the comb drive guides (Figure 3). The guides prevent off-axis motion of the comb drive shuttle during operation of the microengine. The guides had 0.5 µm of lateral play in the design which exhibited linear clamping and 0.25 µm of lateral play in the newer design. The results from the new engine are shown in Figure 7. Equally poor circularity is again observed for both sets of drive equations. However, subtle differences in performance between the two sets of equations may have been masked by friction in the guides. Smaller radii did not yield better circularity.

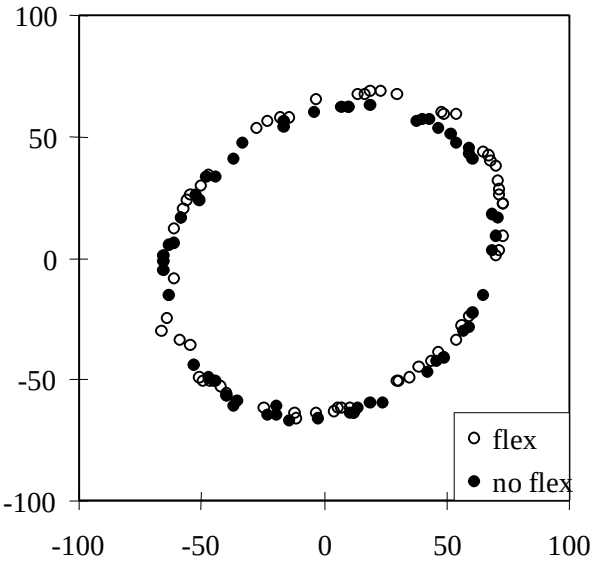

Figure 6. Position map of gearless engine with linear clamping and reduced radius of 12.5 µm. Horizontal and vertical axes are in pixels. 1 pixel » 3 µm.

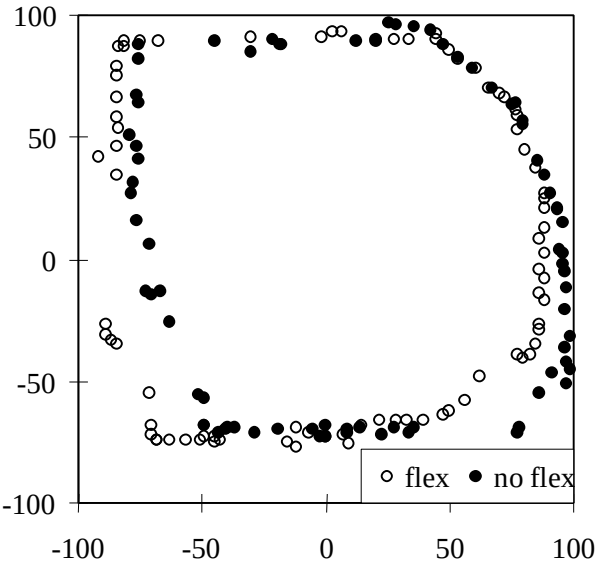

Figure 7. Position map of gearless engine without clamping and radius set to 17 µm. This engine exhibits severe friction at guides. Horizontal and vertical axes are in pixels. 1 pixel » 3 µm.

5. RESONANT FREQUENCY, QUALITY FACTOR

The blur envelope technique described earlier for measuring resonant frequency is labor intensive and has poor resolution. It is generally desirable to have an electrical measurement of the resonant frequency. Electrical measurements are complicated by the presence of large parasitics in the presence of small signals. Nguyen *et al.* [12,13] have reported a technique which has high resolution and can be easily automated. This technique takes advantage of the rate of change of capaciticance with time ($\partial C/\partial t$) of a moving micromechanical structure. This technique is shown schematically in Figure 8 and spectrally in Figure 9. It is a modulation–demodulation scheme, where the electrical signal driving the structure into resonance is first modulated by the structure itself and then demodulated using a mixer.

5.1 Theory

Referring to Figure 8, a drive signal with frequency near the resonance of the structure is applied to the stationary comb fingers. A carrier signal with a DC offset and AC frequency much larger than the resonant frequency of the structure is applied to the shuttle and underlying ground plane. The sense signal is picked off the other set of stationary comb fingers.

The moving shuttle will induce charge on the sense fingers which will give rise to a current. This current is converted to a voltage and amplified by a transimpedance amplifier. Referring to Figure 9(a), the spectral response will contain undesired feedthrough terms at the drive and carrier frequencies w_d and w_c. Modulated sideband terms at $(w_c - w_d)$ and $(w_c + w_d)$ will also be generated. The signal is then passed through a bandpass filter with center frequency near the carrier frequency to eliminate the drive signal component(Figure 9b). It is noted that the drive signal component at this stage is due to unwanted parasitics inherent in the device and measurement scheme itself.

After bandpass filtering, the resultant signal is mixed with the carrier signal that has been phase shifted by 90°. This phase shift has been shown to yield optimal signal amplitude. At this point the spectral components contain peaks at w_d, $2w_c$, $(2w_c - w_d)$, and $(2w_c + w_d)$ (Figure 9c). The height of the peak at w_d is proportional to $(\partial C/\partial t)$ and will increase with increasing amplitude of motion. If the signal after the mixer is fed through a low pass filter, only the w_d peak survives and its height can be monitored with a spectrum analyzer. The spectrum

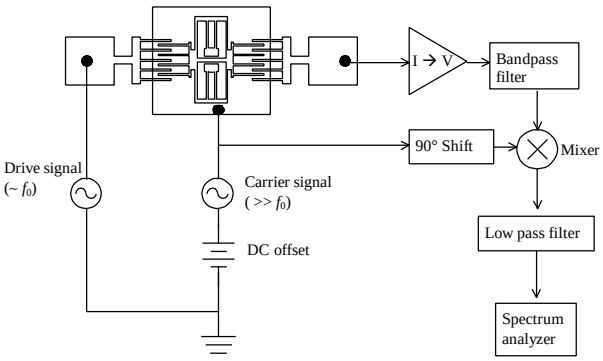

Figure 8. Schematic of modulation–demodulation measurement scheme.

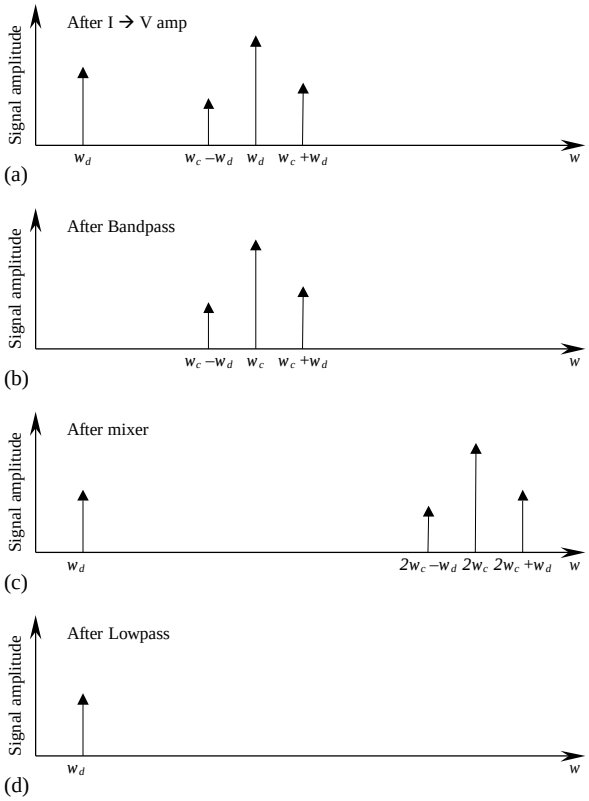

Figure 9. Spectral components graphs from different stages of measurement (a) after I → V amplifier (b) after bandpass filter (c) after mixer (d) after lowpass filter.

analyzer itself can supply the drive signal for the measurement. Used in a swept sine mode, the spectrum analyzer will sweep the drive signal frequency and measure the resultant peak height. In this manner the frequency response of the structure can be measured.

5.2 Measurement Details and Results

An HP3326 dual channel function generator was used to generate the DC offset carrier and phase shifted carrier signals. A dual channel function generator is convenient for performing the phase shifting. A Keithley 428 was used for the transimpedance amplifier. It should be noted that this amplifier can be bandwidth limited at high gains. Passive LC filters from TTE were used for bandpass and lowpass functions. For the mixer, an Analog Devices AD534 chip was used. An HP3562 Dynamic Signal Analyzer was used for acquiring the spectra. It was used in swept sine mode and with a power spectrum display mode. The power spectrum display mode appears to be crucial for obtaining meaningful results.

A carrier frequency of 85.5 kHz and a phase shifted amplitude of 2.5V were used for all measurements. The frequency was sufficiently high enough that the MEMS structures could not respond mechanically to the carrier stimulus. This frequency was chosen as a result of bandwidth limitations of both the transimpedance amplifier and the spectrum analyzer. In general, a higher frequency carrier signal is desirable. Obtaining a meaningful spectrum is highly dependent upon carrier and drive signal amplitudes as well as transimpedance gain. The carrier and drive signal amplitudes are tuned by visually inspecting the device under test to ensure that mechanical oscillation is occurring and that clamping from excessive oscillations does not occur. The output signal from the transimpedance amplifier must be monitored during testing to verify that the maximum gain is used without overloading.

The resultant spectrum of a comb drive identical to those used in the microengine of Figure 1 is shown in Figure 10, with a resonance peak at 1764 Hz. The spectrum near the resonant frequency is shown in Figure 11. An approximate measurement of Q can be obtained from the 3dB bandwidth of the spectrum:

$$Q = \frac{f_0}{f_{3dB}} = \frac{1764}{2298 - 1305} = 1.78 . \qquad (12)$$

This technique has also been applied to a micromachined accelerometer structure which has been reported elsewhere [3,4]. The accelerometer spectrum is shown in Figure 12, and has two peaks. The first peak at 3347 Hz is the real resonance peak, while the second peak, though higher is due to parasitic elements. This figure illustrates the need for visual inspection to verify at what frequency mechanical resonance actually occurs. The blur envelope can be visually monitored during a swept sine measurement to see which peak is a real resonance peak.

6. CONCLUSIONS & FUTURE WORK

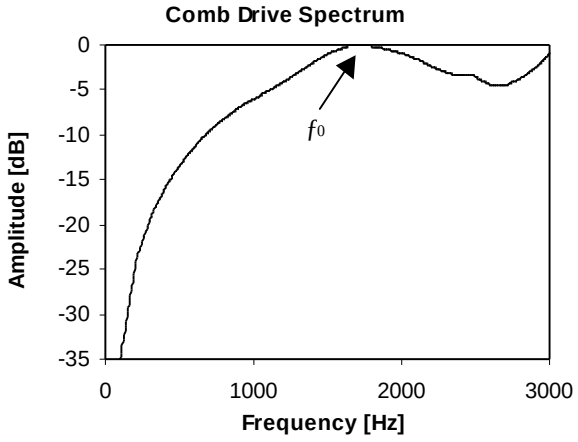

Figure 10. Swept sine power spectrum of microengine comb drive. Drive signal amplitude =5.25 . Carrier signal amplitude(PP) =DC offset = 7.5V.

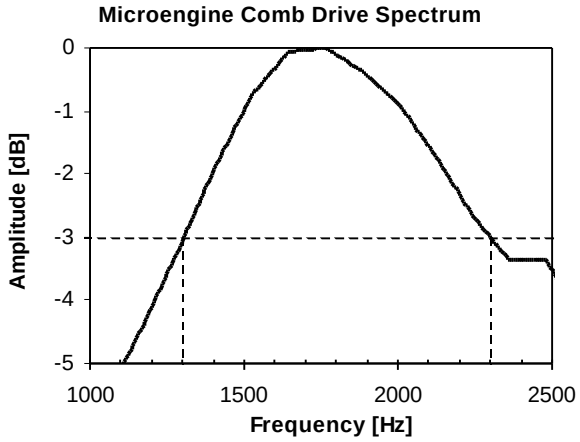

Figure 11. Swept sine power spectrum of microengine comb drive near in the region of resonance. Drive signal amplitude =5.25 . Carrier signal amplitude(PP) =DC offset = 7.5V.

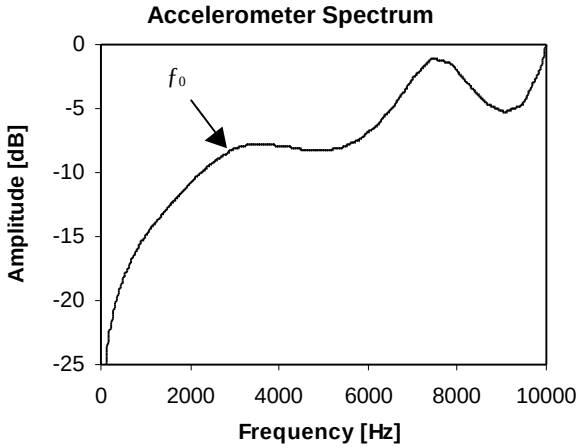

Figure 12. Swept sine power spectrum of accelerometer. Note false peak near 7.5 kHz. Drive signal amplitude =1.4 . Carrier signal amplitude(PP) = 0.7V. Carrier signal DC offset = 0.8V.

Experimental infrastructure has been developed which simplifies characterization of microengines. This infrastructure includes software for calculating ideal drive signals and hardware for applying drive signals and inspecting devices.

Several standard parametric measurements are routinely made which provide information for the fabrication processes: sheet resistance, thin film stress, free beam length, resonant frequency, and microengine functionality.

Applying appropriate drive signals to microengines is critical to optimal performance. A case study was presented on the effect of flex joints. While the flex joint equations exhibited better performance for static measurements, dynamic measurements were inconclusive. This may have been due to linear clamping in one case and excess guide friction in another. A new engine design will be fabricated which does not exhibit linear clamping and has less guide friction, and the flex joint/no flex joint issue will be revisited.

An electrical technique for measuring resonant frequency and quality factor based on work by Nguyen et al. was presented. While this technique is more accurate than using the blur envelope, it does not completely replace optical techniques, since false peaks were observed. Work is under way to extend this measurement scheme to a wider variety of test equipment and to automate the measurement with a Visual Basic program that controls all of the hardware.

ACKNOWLEDGMENT

Sandia is a multiprogram laboratory operated by the Sandia Corporation, a Lockheed Martin Company, for the United States Department of Energy under contract DE-AC04-94-AL85000.

REFERENCES

[1] E. J. Garcia and J. J. Sniegowski, "Surface Micromachined Microengine", *Sensors and Actuators A*, **48** 203-214(1995).

[2] J. J. Sniegowski, "Multi-level polysilicon surface-micromachining technology: applications and issues", ASME 1996 International Mechanical Engineering Congress and Exposition, *Proc. of the ASME Aerospace Division*, AD-Vol. 52, pp. 751-759 (Nov 1996).

[3] http://www.mdl.sandia.gov/micromachine

[4] M. Lemkin, M. Ortiz, N. Wongkomet, B. Boser, and J. Smith, "A Three-Axis Surface Micromachined Sigma-Delta Accelerometer", *Proc. ISSCC*, pp. 202-203 (Feb. 1997).

[5] S. L. Miller, J. J. Sniegowski, G. LaVigne, and P. J. McWhorter, "Friction in Surface Micromachined Microengines", *Proc. SPIE Smart Electronics and MEMS*, **Vol. 2722**, p. 197-204(Feb. 1996).

[6] S. L. Miller, J. J. Sniegowski, G. LaVigne, and P. J. McWhorter, "Performance Tradeoffs for a Surface Micromachined Microengine", *Proc. SPIE Micromachined Devices and Components*, **Vol. 2882**, 1996, p. 182-191(Oct 1996).

[7] J. J. Allen, S. L. Miller, G. F. LaVigne, M. S. Rodgers, and W. P. Eaton, "Dynamic Effects of Linkage Joints in Electrostatic Microengines", Presented at *Modeling and Simulation of Microsystems 1998*, Santa Clara, CA, April 6-8, 1998.

[8] P. Horowitz and W. Hill, *The Art of Electronics*, Cambridge University Press, p. 188 (1989).

[9] D. M. Tanner, N. F. Smith, D. J. Bowman., W. P. Eaton, and K. A Peterson, "First Reliability Test of a Surface Micromachined Microengine Using SHiMMeR", *1997 Symposium on Micromachining and Microfabrication, Proc. SPIE*, **Vol 3224**, pp. 14-23(1997).

[10] D. M. Tanner, W. M. Miller, W. P. Eaton, L. W. Irwin, K. A. Peterson, M. T. Dugger, D. C. Senft, N. F. Smith, P. Tangyunyong, and S. L. Miller, "The Effect of Frequency on the Lifetime of a Surface Micromachined Microengine Driving a Load", *1998 IEEE International Reliability Physics Symposium Proceedings*, pp. 26-35(Mar. 1998).

[11] Y. B. Gianchandani and K Najafi, "Bent Beam Strain Sensors", *Journal of Microelectromechanical Systems"*, **5**(1), pp. 52-58 (Mar 1996).

[12] T.-C. Nguyen, "Electromechical Characterization of Microresonators for Circuit Applications", *Final Report Masters Project*, The University of California at Berkeley, 1991.

[13] C.T.-C Nguyen, " Micromechanical Signal Processors", *Ph.D. Dissertation*, The University of California at Berkeley, 1994.